

Collective formation of misfit dislocations at the critical thickness for equilibrium nanowire heterostructures

Tobias Særkjær^{†,1,2,*} Thue Christian Thann,^{1,2,*} Tomaš Stankevič,² Sergej Schuwalow,^{1,2} Peter Krogstrup^{†1,2}

¹*Center for Quantum Devices, Niels Bohr Institute,
University of Copenhagen, 2100 Copenhagen, Denmark*

²*Microsoft Quantum Materials Lab Copenhagen, 2800 Lyngby, Denmark*

(Dated: February 28, 2025)

In this work we model the evolution of strain energy during different growth stages of heterostructure nanowires. As opposed to a continuous change in the density of dislocations we find the minimum energy configuration changing abruptly, from fully elastically strained to partially relaxed due to collective formation of a misfit dislocation network. These insights are gained from a technique developed to simulate misfit dislocations in a finite element framework, incorporating both elastic and plastic relaxation. We argue that these results have general relevance for heterostructure systems.

I. INTRODUCTION

The presence of misfit dislocations (MDs) in epitaxial heterostructures alters the structural, mechanical, optical and electronic properties. The stress induced from elastic strain, originating from the mismatch between the lattice parameters of a growing thin film and the substrate, acts as a driving force for the formation of structural defects when the critical thickness is exceeded. Understanding the mechanisms that lead to formation of MDs at the critical thickness is therefore important in finding the limits of coherence for engineered epitaxial devices. The transition from elastic to plastic relaxation at the critical thickness in thin films has for these reasons been studied intensively in the past decades, and a number of general models for the formation of MDs have been proposed and tested^{1–14}. Most of these models examine the limit for nucleation of a singular MD in an otherwise elastically strained and pseudo-infinite planar thin film, implicitly assuming singular MD nucleation that form a network of dislocations one at a time.

A challenge with simulating the general case of MD formation for a single interface (pseudo-infinite system) is finding boundary conditions which simplify the model to solvable equations, while not affecting the physics. Using for instance symmetry or periodic boundary conditions will hinder modeling MDs as 'additional' or 'missing' crystal planes in a pseudo-infinite film, since the outer boundaries need the ability to move freely. For this reason we choose Selective Area Growth (SAG) as a model system, as SAG models are not subject to the challenges associated with boundary conditions for pseudo-infinite systems, and SAG offers the opportunity to design complex networks in the plane of the substrate, which makes it a flexible and promising platform for production of scalable quantum devices. For this reason, SAG methods for synthesis of NW heterostructure networks have received increasing interest in the field of quantum devices^{15–22}.

Meanwhile, the initial growth stages of SAG NWs closely resemble the observed trends from planar films, and studies of SAG allow us to probe the mechanisms for MD formation in general.

The non-trivial morphologies found in SAG NWs may be difficult to handle in a purely analytical framework, but they are easily defined with the finite element method (FEM) software employed in our model. Compared to large planar films, SAG morphology may allow the growing film an additional spatial degree of freedom, altering the critical thickness.

Comparing to studies of the free-standing Vapor-Liquid-Solid (VLS) radial type nanowires (NWs), it is shown that the critical thickness can change dramatically^{23–25} due to additional degrees of freedom from the change in morphology with a limited NW radius in the VLS case. Theoretical models^{26,27} attempt to explain this phenomenon from comparison of a fully elastic model and a model exhibiting a single pair of perpendicular, interfacial MDs. The models predict how the critical thickness should scale with parameters such as NW radius and mismatch, and these are nicely summarized in a review by Kavanagh (2010)²⁸. Unfortunately the VLS method lacks reliable ways of forming more complex NW networks in an experimental setting, and so our choice of SAG lets us work with a promising method somewhere between the planar thin film and the VLS NWs.

Starting with the simplest case, we study purely elastic relaxation in SAG NWs to examine the strain energy as a function of growth stages. The shapes studied are those observed in experiments^{15–17}, appearing to be approximately equilibrium shapes given lowest surface energy configuration for the NW cross section. Building on these examinations, we subsequently study elastic and plastic relaxation in SAG NWs with dislocations as 'additional' crystal planes as explained in section III. The FEM simulations are carried out for a wide range of mismatches and MD densities, finding the equilibrium configurations at the critical thicknesses from comparison between the elastic and plastic configurations. We study in particular plastic strain relaxation of a $\langle 110 \rangle$ orientated NW

* These authors contributed equally

on a (001) substrate and buffer, and find a first order-like transition as a function of the extensive parameter film thickness, from a fully elastic configuration to one with a network of MDs formed collectively - a conclusion expected to carry over to other heterostructures subject to in-plane strain caused by a lattice mismatch, depending on the specific morphology and degree of mismatch. Lastly we analyze the equilibrium MD densities and show critical thicknesses and number of MDs as functions of mismatch.

II. PURELY ELASTIC STRAIN RELAXATION

Figure 1a presents a stereographic projection of the typical NW types available on (001) substrates. The purely elastic simulation features a translationally invariant segment, using three symmetry planes as illustrated in figure 1b along with an example of a preliminary mesh. We assume for simplicity that the buffer (region separating the conducting NW channel from the substrate) is relaxed to the underlying substrate. See Supplemental Material for information on strain implementation and calculation of strain energy density (SED) in the FEM software COMSOL²⁹.

Varying geometric parameters allows for analysis of the dependence on dimensions, shape and size of the structure. In an actual growth environment these parameters can be controlled by lithographic patterning and adjusting growth time, flux compositions and temperature. See Supplemental Material for example results of varying size effects.

These simulations are run for an InAs NW on an $\text{In}_{0.75}\text{Ga}_{0.25}\text{As}$ buffer grown in the $\langle 100 \rangle$ direction with $\{110\}$ side facets (see figure 1a). In figure 1c we show three different variations of this morphology, where stage I represents a transport channel grown from a thin layer on the buffer to a full pyramid shape with fully formed facets. We regard this shape to be an approximation of the lowest-energy shape as dictated by the surface energy densities associated with different crystallographic orientations.

The other morphologies represent overgrowth, where stage II A) specifically represents a layer beginning to form on a fully grown stage I NW, and the transition is marked with an arrow in figure 1c. We conclude that for our model, overgrowth contributes to total strain at a lower rate than stage I growth. We also see that stage II B) can accommodate higher mismatch for lower transport channel volumes, but also that this becomes unfavorable at larger channel volumes. All three stages exhibit sublinear increase in total strain energy for very large transport channel volumes. We note that the simulated interface area is kept constant between these morphologies for comparison.

In figure 1d we investigate stage I and stage II B) and the strain energy dependence on the thickness of the InAs layer. For stage II B) we consider only half of the wire

(cut along the axial direction), re-dimensionalized so that the interface area is equal for both morphologies, considered a normalization to interface area. We further compare to a free-standing NW with identical interface area, which is not constrained by symmetry planes. We find this free-standing type NW to be favorable in comparison to SAG at all thicknesses, which is expected since the free-standing NW is less constrained. We note that the graphs for stage I and stage II B) cross each other at approximately 11nm in panel 1d. This is due to stage I gaining less volume per unit layer thickness, as the triangular cross section becomes thinner towards the top. Hence, this crossing is absent in the panel 1c displaying the energy as a function of transport channel volume.

All cases compare favorably to the planar growth of thin film on a planar substrate, which is shown as the dashed line in panel and 1d. The thin film is a rectangular structure with symmetry planes on all four sides to emulate a pseudo-infinite plane. For the thin film case, a mismatch of 1.8% ($\text{InAs}/\text{In}_{0.75}\text{Ga}_{0.25}\text{As}$) corresponds to a critical thickness of $\approx 4.8\text{nm}$ according to Matthews model⁶, depending on the exact Burger's vector in the strained top layer. This highlights the morphological advantages of a SAG buffer, where the NW can relax strain by a rotational degree of freedom which has also been shown by other authors¹⁵.

III. PLASTIC STRAIN RELAXATION

As the crystal volume of a lattice mismatched heterostructure increases during growth, the excess energy increases until a critical thickness is reached, at which point MDs are formed to lower the total energy, most often edge dislocations along the interfaces¹⁵. We are interested in understanding the limits of fully elastically strained heterostructures as a function of shape, volume and composition (which defines the lattice mismatch).

In a simple 1-dimensional case, the spacing between dislocations is generally given by: $d = |b|/(\delta - \varepsilon)$, with $|b|$ being the length of the Burger's vector, δ being the mismatch and ε being the average remaining elastic strain. Therefore 'full plastic relaxation' corresponds to $\varepsilon = 0$ with a corresponding density of dislocations. However, there will be a certain fraction of elastic vs. plastic relaxation that will display the minimum strain energy, and we can not in general expect full plastic relaxation. If we wish to engineer structurally defect-free NWs, we need to examine configurations with different MD densities in order find the equilibrium configuration at the critical thickness.

Figure 2d shows a model of a $\langle 110 \rangle$ type NW with edge MDs of in-plane Burger's vectors of type $\frac{a}{2}\langle 110 \rangle$, where a is the lattice parameter. The dislocations are here modeled as planes in the buffer with thickness matching the length of the Burger's vector and positive unity strain (normal to the planes) simulating 'additional' crystal planes due to misfit dislocations at the interface. This

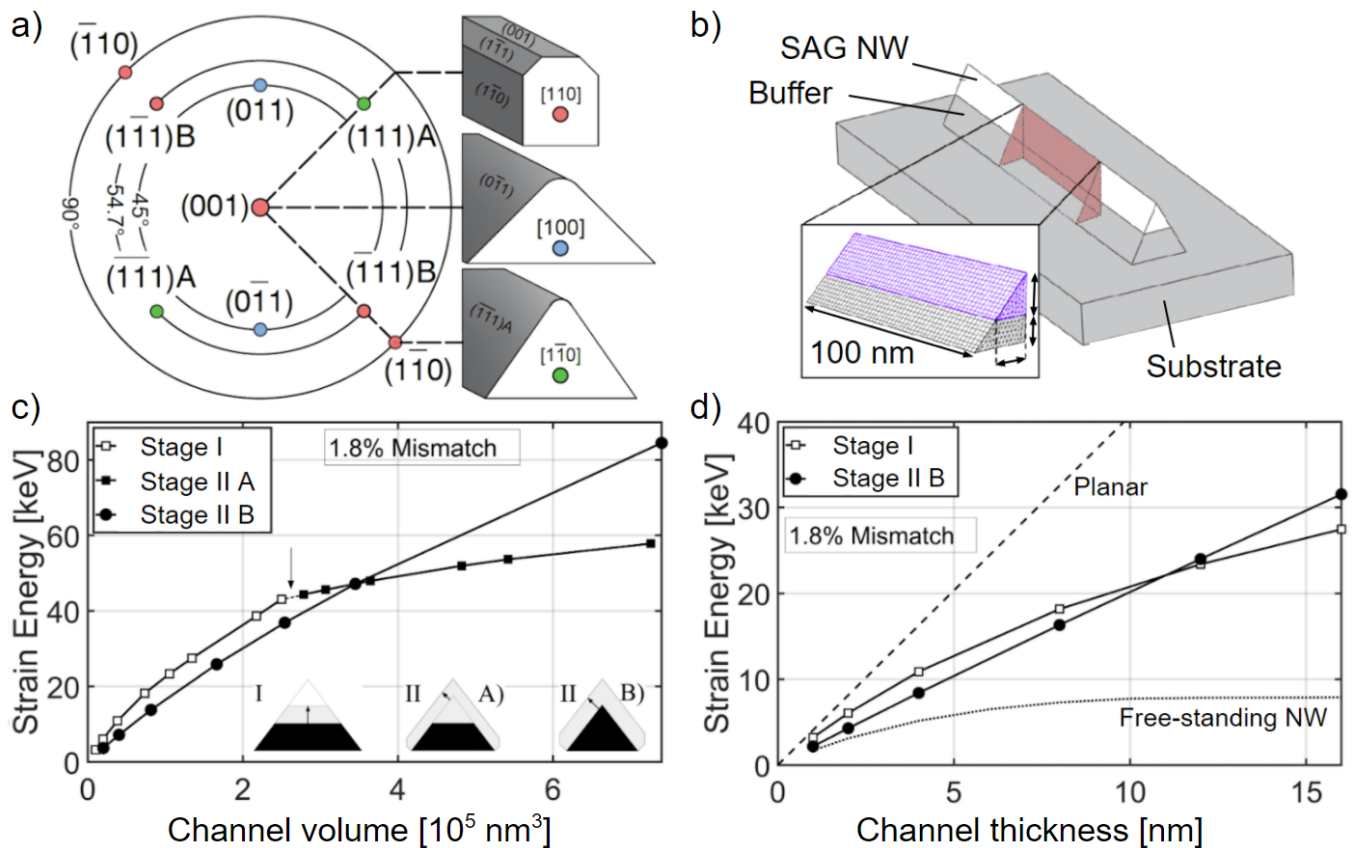


Figure 1: **Elastic growth of translationally invariant NWs.** **a)** Linear stereographic projection of SAG NWs grown on (001) substrate. **b)** Sketch of a SAG NW on a substrate with indicated symmetry planes, and a mesh example in zoom-in. **c)** Total elastic strain energy per 100 nm section length of a $\langle 100 \rangle$ NW as a function of InAs transport channel volume V_{InAs} on a $\text{In}_{0.75}\text{Ga}_{0.25}\text{As}$ buffer (approx. 1.8% mismatch). Insets (InAs: grey, InGaAs: black) illustrate three types of cross sectional shapes. Growth stages are described further in the main text. **d)** As c) except investigated as a function of transport channel thickness h_{InAs} , where the dotted line represents a free-standing NW model at same mismatch and interfacial area. The free-standing NW is simulated as hexagonal in cross-section, protruding normal to a $\{111\}$ substrate. We consider only half a stage II B) NW, as the two sides have little to no strain field interplay.

ensures the correct effect of MDs in the transport channel, but leaves artifacts in the simulations of the buffer and substrate where the 'additional' planes should not in general be strained relative to the surrounding material far from the interface. We emphasize that this method works for finite-size structures such as the SAG morphologies chosen here, and conversely this method is incompatible with simulations of pseudo-infinite systems using fixed position symmetry planes, because they inhibit the strain-relaxing displacement generated by the additional crystal planes.

An alternate method simulates the same dislocations as 'missing' planes in the transport channel with negative unity strain (figure 2e). This creates the correct effect in the buffer and substrate, while the unwanted artifacts are now found in the transport channel as the fixed position symmetry planes again inhibit displacement. The dislocation planes end at the NW-buffer interface where the dislocations are situated¹⁵. In panels 2a-c we compare

these two methods to the analytical solution of stress fields associated with dislocations at the interface of two semi-infinite solids in 2D as found by Head (1953)³⁰, which combined with mesh convergence studies give us confidence that we have reached a sufficient resolution. While we find a clear convergence in the elastic simulations at cell sizes of 10-20nm, the plastic cases have domains around the dislocations reaching convergence just under 1nm and being simulated at a maximum of 0.01nm. The two methods can be combined graphically to yield the results shown in figure 2h, with a complete solution being to run both simulations and consider in each only the correctly affected domains. Since by far the biggest contribution to the strain energy ($\approx 99\%$) is found in the transport channel, on top of the buffer, we continue only with the MD model first described (figure 2d)

As seen in figure 2a-c, a small region around the dislocation cores becomes very highly strained. As a result, the elastic theory employed for evaluation of the SED is lo-

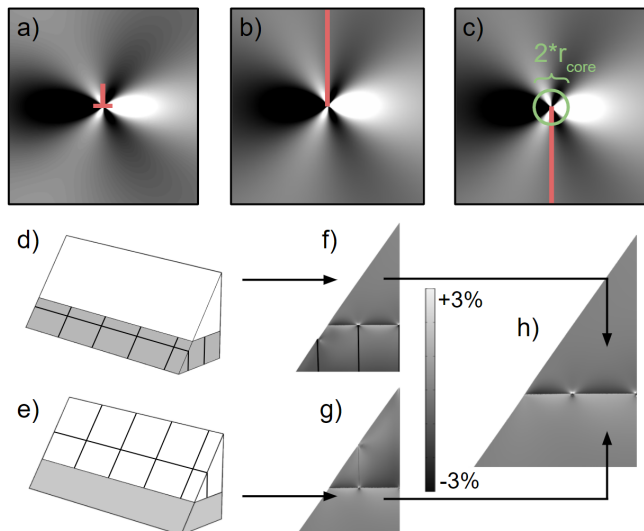


Figure 2: **FEM simulations of dislocations.** Top row: XY-components of stress fields caused by an edge dislocation at the markers. **a)** Analytical solution by Head³⁰. **b)** and **c)** Results from 2D FEM simulations with dislocations modeled as a planes indicated by markers, with strain (+1) and (-1) respectively. Panel **c)** additionally shows the region near the core excluded from energy calculations, size exaggerated for clarity. **d)** and **e)** 3D FEM models of $\langle 110 \rangle$ type NW (substrate not shown) with $\frac{a}{2}\langle 110 \rangle$ dislocations modeled as vertical planes with strain (+1) and (-1), respectively. **f)** and **g)** Horizontal components of strain resulting from models **d)** and **e)** with 3% mismatch (InAs/In_{0.58}Ga_{0.42}As). **h)** Composite image of results from the two models in panels **f)** and **g)**.

cally no longer valid, and an alternate method is needed if one wishes to evaluate the strain energy included in regions near the dislocations. The 'Volterra method'¹ or 'empirical method'³¹ of excluding small cylindrical cores (see figure 2c) from SED integrations to account for singularities and the reconstruction of chemical bonds at the dislocation cores works well for dislocations surrounded by a larger body of material¹, but in thin films the strain fields near the dislocation cores interact with the free surface, effectively making the radius of this small excluded core a non-trivial function of the mismatch and morphology.

Our simulations were carried out using models of the type in figure 3a (interface width 125nm, channel length 4 μ m), with 'transverse' dislocations as equidistantly spaced 'additional' planes in the substrate and then buffer. The orientation was chosen with $\langle 110 \rangle$ along the NW axis and $\{111\}$ type side facets (see figure 1a). The material composition of the buffer was varied with corresponding changes in material parameters according to Vegard's Law, and chosen to emulate mismatches from 1% to 4% corresponding to InAs on In_xGa_{1-x}As with x between 0.86 and 0.44. In all cases the composition within each region (substrate, buffer, NW) was chosen as spatially

uniform for simplicity. The thickness of the thin film was varied (akin to the method employed for figure 1d) to emulate different stages of approximate layer-by-layer growth throughout.

We are concerned with the total strain energy in the transport channel (NW), which comprises by far the dominant energy contribution compared to the buffer and substrate. In order to evaluate the 'invalid regions' mentioned above, we modify the 'Volterra method' by excluding slightly larger cylindrical cores of radius $r_{core} = |b|/2$, with b being the Burger's vector, arguing that the dominant energy contribution inside this range is due to the rearrangement of chemical bonds. We account for these bonds by adding an energy per unit dislocation length from the melting approximation given as $E_m = Gb^2/2\pi$ where G is the shear modulus of the transport channel, in this case InAs.

IV. RESULTS

Figure 3b shows the strain energy of plastic configurations in units of the strain energy for the purely elastic configuration as a function of film thickness for a mismatch of $\delta = 2\%$. See Supplemental Material for similar results for other mismatches.

From closer examination it becomes obvious, that the first plastic configuration to become favorable is not the one with a singular dislocation. This is a general feature across the mismatches examined, but more notable for higher mismatches. This suggests that nucleation of dislocations at the critical thickness is a first order-like transition in an extensive parameter, to a state which becomes stable when a certain equilibrium MD density is achieved.

In this study we have limited ourselves to one axial dislocation running along the center of the NW, and note that a more complete examination would have to deal with a much larger parameter space of both number and positions of axial MDs.

We also note the general feature that higher mismatches tend to favor configurations with more MDs. For the 1% mismatch case the equilibrium configuration at the critical thickness has only transverse dislocations (MD_{\perp}), which could be interesting for engineering of MDs in heterostructures. However, for the mismatches of 2%, 3% and 4% the equilibrium configurations at the critical thicknesses have both the axial and transverse dislocations present. This could prove useful for analysis, as the lack of an axial MD from cross sectional TEM of a high mismatch structure could indicate that the entire structure is purely elastically relaxed.

The question of MD configuration at the critical thickness is examined further in figure 4a which shows the points where different configurations become favorable compared to the purely elastic case. For a given mismatch the lowest of the critical thicknesses is the predicted equilibrium critical thickness, and a specific MD

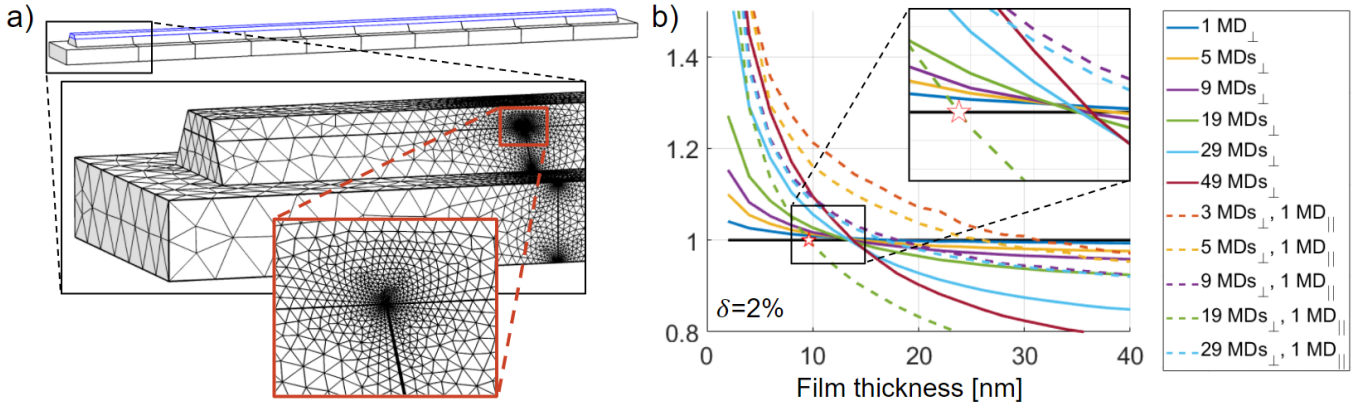


Figure 3: **Model and strain energy as function of film thickness.** a) Model along with a zoom section displaying a preliminary mesh with increased density near the dislocations. b) Total strain energy of different plastic configurations in units of the elastic configuration at the corresponding film thickness for a mismatch of $\delta = 2\%$. Note that the first plastic configuration to become favorable compared to the elastic case displays a network of MDs rather than one singular MD. The dimensions of the interface in the model are 125nm by 4 μ m.

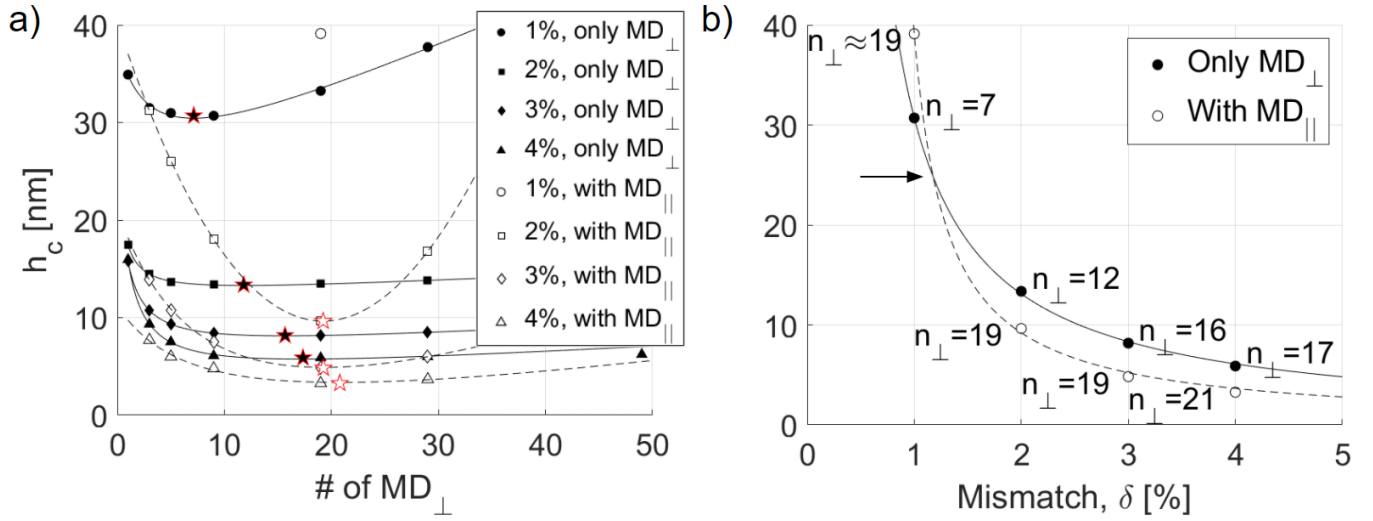


Figure 4: **Fitting critical thicknesses.** Panel a) shows the predicted critical thicknesses, assuming a set number of dislocations for each of the four mismatches. Markers denote minima from fits. Panel b) shows the minima from a) for each mismatch (δ) along with the corresponding number of dislocations found from fits. Fit types are described in the main text. The dimensions of the interface in the model are 125nm by 4 μ m.

density is associated with this.

The guidelines in figure 4a are fits to the form $h_c = an_{disl} + b + c/(n_{disl} + d)$, where n_{disl} is the number of dislocations. The minima from figure 4a (marked) are extracted from the fits and plotted in figure 4b along with the associated number of MDs and new fits of the simpler form $h_c = \alpha/(\delta + \beta)$ where δ is again the mismatch.

The variables $\alpha_{\perp} = 22.8\text{nm}$, $\beta_{\perp} = -0.26\%$, $\alpha_{\parallel} = 12.1\text{nm}$, and $\beta_{\parallel} = -0.69\%$ are found from the fits for configurations without and with the axial dislocation, respectively. Notably, for mismatches below $\delta_{\parallel}^* = 1.2\%$, the configuration at the critical thickness shows no axial dislocation.

The fit forms and variables found suggest a divergence of the critical thickness at a mismatch of a quarter of a percent. However, to ensure a fully elastic growth in stage 1, we would merely need the critical thickness to be larger than the thickness of the transport channel grown. Due to the geometry chosen for the model, the stage 1 transport channel can grow to a maximum thickness of $h_{max} = w/\sqrt{2}$, where $w = 125\text{nm}$ is the width of the interface. From the model, this can be accommodated elastically at a mismatch of $\delta^* = 0.52\%$ or InAs on In $_{0.93}$ Ga $_{0.07}$ As, although a buffer this high in In composition would probably cause issues in terms of properly containing the wave function to the intended transport channel.

Finally we note that while all the critical thicknesses quoted are specific to the morphology, dimensions and materials examined, the method presented can be used for examination of other combinations.

V. DISCUSSION AND CONCLUSION

We find the mechanisms of strain relaxation in lattice mismatched SAG NW heterostructures are shown to be distinctly different from planar heterostructures as well as from free-standing NW heterostructures^{26,27}. Compared to planar thin films, the additional elastic relaxation for SAG stems from the rotational degree of freedom for relaxation transverse to the NW axis which in principle can overshoot the bulk relaxed values, giving additional room for elastic relaxation along the NW axis through the Poisson effect. We identify three different growth stages, all of which are energetically favorable compared to planar thin film growth, and all of which are sublinear but quickly become approximately linear with different dependencies on layer thickness, favoring stage II A).

Our findings establish a relationship between transport channel layer thickness and MD density for a SAG NW morphology, similar to that between NW radius and misfit percentage as found by Ertekin *et al.* (2005)²⁶ and Glas (2006)²⁷ for VLS NWs. This highlights the difference between SAG and free-standing NWs. For comparison we quote the experimentally found critical thickness of $h_{c, \text{film}\%} = 1.71\text{nm}$ for planar thin film growth of InP on GaAs at 3.8% lattice mismatch³². This shows the ability for elastic relaxation in SAG NWs as somewhere between the highly constrained planar thin films and the nearly unconstrained free-standing NWs of VLS.

We compare to previous efforts in using FEM to analyze misfit dislocations such as Ye *et al.* (2009)³³, which also use initial strain as a numeric technique, but fails to include both elastic and plastic relaxation simultaneously and naturally does not take the spatial freedoms and lattice directions of SAG NWs into account. Therefore we believe our methods are novel and relevant for finite-size morphologies across materials, and the results can be compared to physical samples by analysis of e.g. atomic resolution TEM with GPA.

It is appropriate to discuss this abrupt and collective formation in relation to observed formations. As done by LeGoues *et al* (1994)³⁴, UHV TEM can be used *in situ* to observe singular MD formations in island growths, with accompanying changes in growth velocity immediately before and after nucleation events. They provide rudimentary theoretical considerations with equilibrium assumptions, but we consider their model incomplete as it does not include strain energy as a driving force and does not explain the preference for island growth over layer-by-layer. We understand that in our study we have specifically simulated an equilibrium environment, and created a rigorous framework incorporating strain energy

and additional references.

A later study by Merdzhanova *et al* (2006)³⁵ uses a more time-efficient AFM method, and notes higher growth temperatures consistently giving rise to more singular nucleation events, as well as a dramatic change in the size of islands. Particularly the balance between coalescence of neighbouring islands growing simultaneously, as opposed to islands growing smaller when located in the depletion zone of a larger island, is affected. They do not present a complete theory for this behavior, but suggest a scenario qualitatively involving material intermixing.

We note these points to be different from the assumptions within our model, and that temperature dependencies agree well with a non-equilibrium nature of the process. As such we find the discrepancies to our model as expected, and they underline the potential in understanding the equilibrium and non-equilibrium divide in phenomena and behavior. In particular, the role of material intermixing could be introduced and studied within our framework, posing an immediate candidate for further work.

In summary we present a novel method for introducing plastic relaxation from MDs as localized FEM model features in heterostructure simulations, allowing an examination covering different morphologies and MD densities. This leads to our prediction of collective rather than singular onset of MDs at the critical thickness, which we consider a novelty. For SAG NW growth in stage I, we find critical thicknesses of $h_{c,1\%,\perp} = 30.7\text{nm}$, $h_{c,2\%,\parallel} = 9.6\text{nm}$, $h_{c,3\%,\parallel} = 4.8\text{nm}$, and $h_{c,4\%,\parallel} = 3.3\text{nm}$ for 1%, 2%, 3%, and 4% mismatch, respectively, as summarized in figure 4. In all cases we find that collective formation, as a first order-like transition as a function of film thickness, is favorable compared to singular onset. For mismatches below $\delta_{\parallel}^* = 1.2\%$ we find that the equilibrium configuration shows only transverse dislocations, while for mismatches above this value both axial and transverse dislocations are expected. We argue that our results are relevant for general heterostructures, predicting that a first order-like transition in our finite-size case carries over to e.g. a pseudo-infinite planar heterostructure. As discussed in III there is agreement with the analytical solution for semi-infinite planes, while it is not possible to use fixed position symmetry planes, because they create unphysical effects when introducing misfit dislocations.

ACKNOWLEDGEMENTS

This paper was supported by Microsoft Station Q, and by the European Research Council (ERC) under grant agreement No. 716655 (HEMs-DAM).

The authors thank Martín Espiñeira, Daria Beznasyuk, Anna Wulff Christensen, Filip Křížek, Thomas Kanne, Joachim Sestoft, Jordi Arbiol, Sara Martí-Sánchez, and Philippe Caroff for shared data, fruitful discussions and academic and practical inputs.

- ¹ J. H. van der Merwe *Misfit Dislocation Generation in Epitaxial Layers*, Critical Reviews in Solid State and Materials Sciences, 17(3), CRC Press, Inc. (1991)
- ² F. C. Frank and J. H. van der Merwe *One-Dimensional Dislocations. I. Static Theory*, Proc. R. Soc. Long. A, **198**, 205-216, (1949)
- ³ J. H. van der Merwe *Crystal Interfaces. Part I. Semi-Infinite Crystals*, Journal of Applied Physics, **34**, 1, (1963)
- ⁴ J. H. van der Merwe *Crystal Interfaces. Part II. Finite Overgrowths*, Journal of Applied Physics, **34**, 1, (1963)
- ⁵ J. W. Matthews and A. Blakeslee *Defects in epitaxial multilayers: I. Misfit dislocations*, Journal of Crystal Growth, **27**, 118-125 (1974)
- ⁶ J. W. Matthews *Defects associated with the accommodation of misfit between crystals*, Journal of Vacuum Science and Technology, 12(1), 126-133 (1975)
- ⁷ R. People and J. C. Bean *Calculation of critical layer thickness versus lattice mismatch for Ge_xSi_{1-x}/Si strained-layer heterostructures*, Appl. Phys. Lett. **47**, 322 (1985)
- ⁸ B. W. Dodson and J. Y. Tsao *Relaxation of strained-layer semiconductor structures via plastic flow*, Appl. Phys. Lett. **51**, 1325 (1987)
- ⁹ J. Y. Tsao, B. W. Dodson, S. T. Picraux, and D. M. Cornelson *Critical Stresses for Si_xGe_{1-x} Strained-Layer Plasticity*, Phys. Rev. Lett. **59**, 21 (1987)
- ¹⁰ E. A. Fitzgerald *Dislocations in strained-layer epitaxy: theory, experiment, and applications*, Mater. Sci. Reports **7**, (1991) 87
- ¹¹ D. J. Dunstan *Strain and strain relaxation in semiconductors*, Journal of Materials Science: Materials in Electronics **8**, 337, (1997)
- ¹² B. W. Dodson and J. Y. Tsao *Relaxation of strained-layer semiconductor structures via plastic flow*, Appl. Phys. Lett. **51**, 1325 (1987)
- ¹³ J. Y. Tsao, B. W. Dodson, S. T. Picraux, and D. M. Cornelson *Critical Stresses for Si_xGe_{1-x} Strained-Layer Plasticity*, Phys. Rev. Lett. **59**, 21 (1987)
- ¹⁴ P. M. J. Maré, J. C. Barbour, J. F. van der Veen, K. L. Kavanagh, C. W. T. Bulle-Lieuwma, and M. P. A. Viegors *Generation of misfit dislocations in semiconductors*, Journal of Applied Physics, **62**, 4413 (1987)
- ¹⁵ F. Krizek, J. E. Sestoft, P. Aseev, S. Marti-Sanchez, S. Vaitiekėnas, L. Casparis, S. A. Khan, Y. Liu, T. Stankevič, A. M. Whitar, A. Fursina, F. Boekhout, R. Koops, E. Uccelli, L. P. Kouwenhoven, C. M. Marcus, J. Arbiol, P. Krogstrup *Field effect enhancement in buffered quantum nanowire networks*, Physical Review Materials **2**, 093401 (2018)
- ¹⁶ S. Vaitiekėnas, A. M. Whitar, M.-T. Deng, F. Krizek, J. E. Sestoft, C. J. Palmstrøm, S. Marti-Sanchez, J. Arbiol, P. Krogstrup, L. Casparis, C. M. Marcus *Selective-Area-Grown Semiconductor-Superconductor Hybrids: A Basis for Topological Networks* Phys. Rev. Lett., 121, 147701 (2018)
- ¹⁷ J. S. Lee, S. Choi, M. Pendharkar, D. J. Pennachio, B. Markman, M. Seas, S. Koelling, M. A. Verheijen, L. Casparis, K. D. Petersson et al., *Selective-area chemical beam epitaxy of in-plane InAs one-dimensional channels grown on InP(001), InP(111B), and InP(011) surfaces* Phys. Rev. Materials **3**, 084606 (2019)
- ¹⁸ M. Friedl, K. Cerveny, P. Weigele, G. Tütüncüoğlu, S. Martí-Sánchez, C. Huang, T. Patlatiuk, H. Potts, Z. Sun, M. O. Hill et al., *Template-Assisted Scalable Nanowire Networks*, Nano Lett. **18**, 2666-2671 (2018)
- ¹⁹ M. Fahed, L. Desplanque, D. Troadec, G. Patriarche, X. Wallart *Selective area heteroepitaxy of GaSb on GaAs (001) for in-plane InAs nanowire achievement*, Nanotechnology **27**, 505301 (2016)
- ²⁰ L. Desplanque, M. Fahed, X. Han, V. K. Chinni, D. Troadec, M-P. Chauvat, P. Ruterana, X. Wallart *Influence of nanoscale faceting on the tunneling properties of near broken gap InAs/AlGaSb heterojunctions grown by selective area epitaxy*, Nanotechnology **25**, 465302 (2014)
- ²¹ P. Aseev, A. Fursina, F. Boekhout, F. Křížek, J. E. Sestoft, F. Borsoi, S. Heedt, G. Wang, L. Binci, S. Martí-Sánchez et al., *Selectivity map for molecular beam epitaxy of advanced III-V quantum nanowire networks*, Nano Letters, 19, 1, 218-227 (2019)
- ²² R. het Veld, D. Xu, V. Scahller, M. Schaller, M. A. Verheijen, S. Peters, J. Jung, C. Tong, Q. Wang, M. de Moor, B. Hesselmann et al., *In-plane selective area InSb-Al nanowire quantum networks* Communications Physics, 3, 59 (2020)
- ²³ B. J. Ohlsson, M. T. Björk, A. I. Persson, C. Thelander, L. R. Wallenberg, M. H. Magnusson, K. Depptert, and L. Samuelson *Growth and characterization of GaAs and InAs nano-whiskers and InAs/GaAs heterostructures*, Physica E **13**, (2002) 1126-1130
- ²⁴ K. Kavanagh, I. Saveliev, M. Blumin, G. Swadener, and H. Ruda *Faster radial strain relaxation in InAs-GaAs core-shell heterowires*, Journal of Applied Physics **111**, (2012) 044301
- ²⁵ A. Biermanns, T. Rieger, G. Bussone, U. Pietsch, D. Grützmacher, and M. Ion Lepsa *Axial strain in GaAs/InAs core-shell nanowires*, Applied Physics Letters **102**, (2013) 043109
- ²⁶ E. Ertekin, P. A. Greaney, D. C. Chrzan, et al., *Equilibrium limits of coherence in strained nanowire heterostructures*, J. Appl. Phys. **97**, (2005) 114325
- ²⁷ F. Glas *Critical dimensions for the plastic relaxation of strained axial heterostructures in free-standing nanowires*, Phys. Rev. B **74**, (2006) 121302(R)
- ²⁸ K. Kavanagh *Misfit dislocations in nanowire heterostructures*, Semicond. Sci. Technol. **25**, (2010) 024006
- ²⁹ COMSOL Multiphysics 5.4 Documentation, COMSOL Inc., www.comsol.com/documentation, October 3 2018 *Structural Mechanics Module*
- ³⁰ A. K. Head *Edge Dislocations in Inhomogenous Media*, Proc. Phys. Soc. B **66**, 793 (1953)
- ³¹ J. P. Hirth and J. Lothe *Theory of Dislocations*, Wiley (1982)
- ³² A. Mazuelas, L. González, F.A. Ponce, L. Tapfer, F. Briones *Critical thickness determination of InAs, InP and GaP on GaAs by X-ray interference effect and transmission electron microscopy*, Journal of Crystal Growth, 131, Elsevier (1993)
- ³³ H. Ye, P. Lu, Z. Yu, Y. Song, D. Wang and S. Wang *Critical*

Thickness and Radius for Axial Heterostructure Nanowires Using Finite-Element Method, Nano Letters **9**, 5 1921-1925 (2009)

³⁴ F.K. LeGoues, M.C. Reuter, J. Tersoff, M. Hammar and R.

M. Tromp *Cyclic growth of Strain-Relaxed Islands*, Physical Review Letters **73**, 2 (1994)

³⁵ T. Merdzhanova, S. Kiravittaya, A. Rastelli, M. Stoffel, U. Denker and O.G. Schmidt *Dendrochronology of Strain-Relaxed Islands*, Physical Review Letters **96**, 226103 (2006)

Supporting Information: First order transition in equilibrium misfit dislocation network formation

Tobias Særkjær^{†,1,2,*} Thue Christian Thann,^{1,2,*} Tomaš Stankevič,² Sergej Schuwalow,^{1,2} Peter Krogstrup^{†1,2,†}

¹Center for Quantum Devices, Niels Bohr Institute,
University of Copenhagen, 2100 Copenhagen, Denmark

²Microsoft Quantum Materials Lab Copenhagen, 2800 Lyngby, Denmark

(Dated: February 28, 2025)

I. COMSOL MODELS FOR FEM SIMULATION

Our FEM simulations were carried out as 3-dimensional Stationary studies with the Solid Mechanics part of the Structural Mechanics module in COMSOL Multiphysics¹. Materials in COMSOL can be defined with a variety of different properties, either from scratch or from a library of predefined materials. The important properties are the Bulk Modulus, Poisson ratio and elasticity matrix. The entries of the elasticity matrix are used for calculations of strain energy density from linear elastic theory. The Linear Elastic Material sub-menu of the Solid Mechanics part of the interface allows for imposing initial strain in select parts of any geometry built.

Initial tensile strain is employed (in-plane with the interface) in the NW corresponding to a chosen lattice mismatch between NW and the buffer, from which a balance of forces on each mesh point yields the final configuration with forced coherence at the interface.

The strain energy density (SED) is found locally from derivatives of the displacement according to equation 1:

$$U_{SED} = \sum_{ijkl} \frac{1}{2} c_{ijkl} \varepsilon_{ij} \varepsilon_{kl} \quad (1)$$

with c_{ijkl} being the stiffness coefficients and ε_{ij} components of the strain tensor. Evaluations of the resulting strain must properly account for the initial strain imposed.

The relevant bulk parameters are the lattice and elastic constants and for $\text{In}_x\text{Ga}_{1-x}\text{As}$, where we assume linear interpolation between the respective parameters^{2,3} of the component materials (Vegard's law).

Some drawbacks do arise from the static and continuous simulations of a dynamic and atomistic physical system, and we should address those here. Drawbacks include but are not limited to a lack of polarity, static elasticity and lattice constants, and uniform compositions within each region. While these drawbacks are relevant

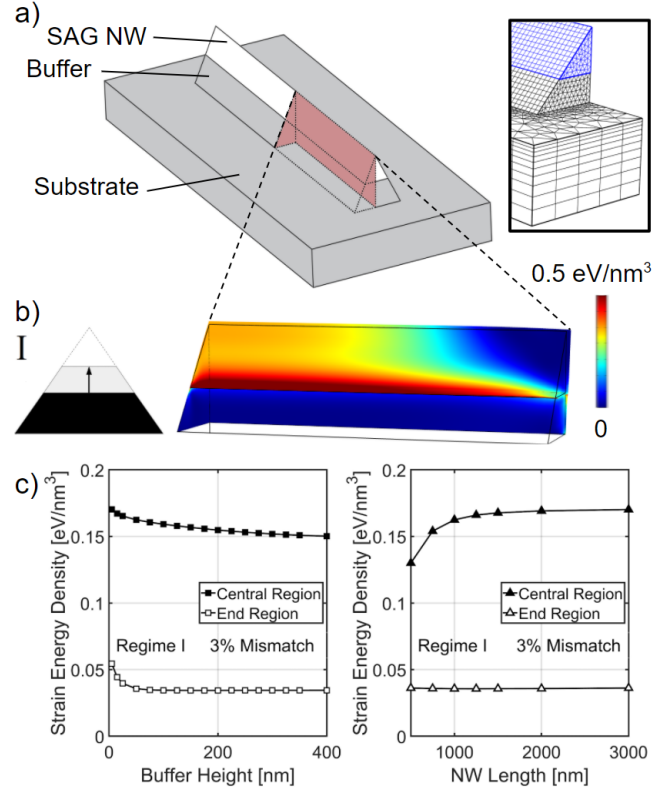


Figure S1: **Finite length effects, 3% mismatch (InAs/In_{0.58}Ga_{0.42}As).** **a)** Illustration of end section with symmetry planes. **Box:** Example mesh of end section. **b)** Distribution of strain energy density on buffer-NW interface as well as both symmetry planes for a fully triangular shaped NW (fully grown stage I). **c)** Strain energy in a central cube as a function of size parameters, showing length scales for decoupling of the center to the end effects.

and present, plenty of results are still obtainable, and simulations of strain relaxation and dislocations in SAG heterostructures could prove a central tool for achieving dislocation free, scalable, high mobility devices.

* These authors contributed equally

† krogstrup@nbi.ku.dk

II. FINITE LENGTH EFFECTS

Turning our attention to the regions near the NW ends, figure S1a shows a NW morphology for stage I growth with only two symmetry planes imposed to examine finite length and the corresponding gradient in elastic strain energy density towards the end of the NW.

The translationally invariant NW segments investigated in the main text relax strain primarily by rotation of crystal planes in directions perpendicular to the NW axis. Near the ends of the NWs, rotation along the NW axis provides an additional degree of freedom for relaxation. Figure S1b shows the distribution of SED in the stage I model. Unsurprisingly, the general trend shows a higher SED near the interface tapering off with distance. For the stage I growth we see the SED decreasing as we move from the middle towards the NW sides.

Figure S1c shows a comparison of the average strain energy density of 50nm sections in the center and end of the NW. The simulations are run for a $\langle 100 \rangle$ type NW at 3% mismatch ($\text{InAs}/\text{In}_{0.58}\text{Ga}_{0.42}\text{As}$) NW, and we investigate the geometric parameters of NW length and buffer height.

We notice a clear trend of the end region converging faster and at lower values. We also see target dimensions of a buffer in order to minimize strain energy. This method can be employed for examination of parameters in both fully elastic and plastic configurations.

III. STRAIN FRAMEWORK

For pedagogical reasons, the main paper and this supplemental is phrased in terms of linear strain, that is:

$$\varepsilon_l = \frac{L}{L_0} - 1 \quad (2)$$

with ε_l being the linear strain and L being the final length of an object with unstrained length L_0 . In this linear strain framework, the strain is just the fractional elongation of the object. The reader should note, that several frameworks for strain are available, and notably that strain in the Solid Mechanics module of COMSOL¹ is Green-Lagrange strain:

$$\varepsilon_{GL} = \frac{1}{2} \left[\left(\frac{L}{L_0} \right)^2 - 1 \right] \quad (3)$$

Other FEM packages may employ different strain frameworks, and adequate adjustments should be taken to account for this. E.g. we note that $\varepsilon_l = +1$ corresponds to $\varepsilon_{GL} = 3/2$, while $\varepsilon_l = -1$ corresponds to $\varepsilon_{GL} = -1/2$. For the purposes of this supplemental, we shall continue to phrase strain in the linear terms, since it allows for a more intuitive understanding, keeping in mind that the specific implementation is recast depending on the strain framework of the FEM software.

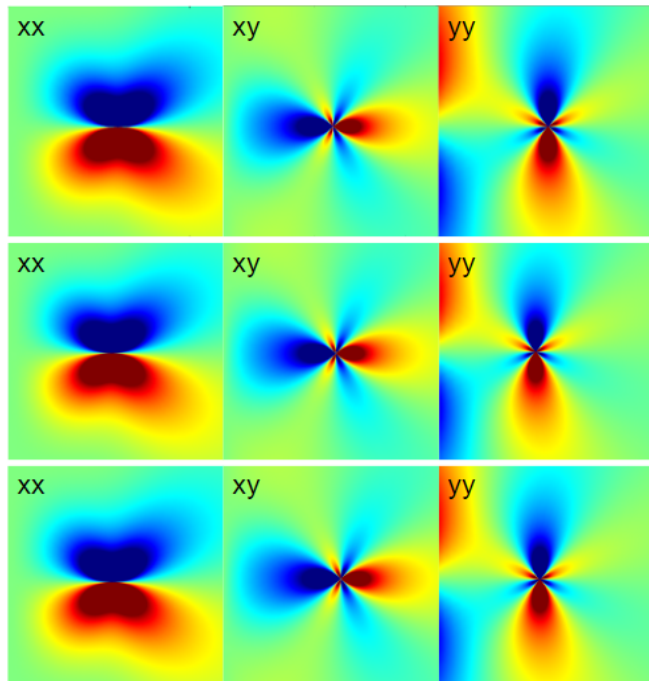


Figure S2: Stress components caused by an edge dislocation near a fixed surface (left side). Top row: Analytic solution by Head⁴. Mid row: Simulation using (+1) strain method. Bottom row: Simulation using (-1) strain method. The middle column is also shown in the main text.

IV. ANALYTIC SOLUTION AND METHOD EQUIVALENCE

The default simulation including MDs modeled as planes with +1 strain in the buffer, corresponding to the 'additional' crystal planes. As mentioned in the main text, this ensures correct boundary conditions from the interface and above, while the boundary conditions inside the lower part are obviously incorrect, since the imposed planes are not actually strained compared to the surrounding material, as confirmed in e.g. geometric phase analysis of atomic resolution TEM. This method is especially viable, since we are mostly concerned with the variations in the transport channel. Equivalently we can model the MDs as planes with -1 strain in the wire, corresponding to the 'missing' crystal planes. This method ensures correct boundary conditions from the interface and below.

The simulation results should agree with analytic solutions, e.g. solutions by Head⁴. Fig. S2 shows different components of a 2D stress fields caused by an edge dislocation, as analytic solution or modeled by the methods mentioned above. The figure shows a clear equivalence between all three methods, validating the simulational method. For the purposes of our simulation the concept is straight forwardly extended to three dimensions.

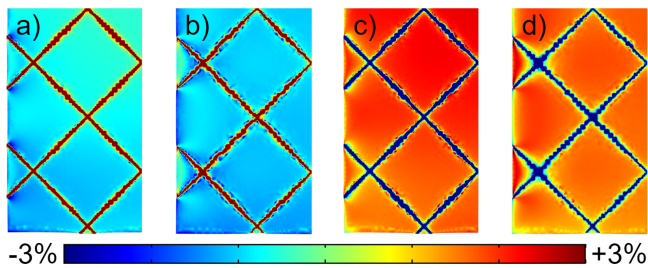


Figure S3: Top views of a section of the NW at the interface between NW and buffer for a $\{100\}$ type NW. a) Transverse (horizontal) strain component using the method with +1 strain in the buffer. b) Same as a, using the method with -1 strain in the NW. c) Out of plane strain component, +1 strain method. d) Same as c, using -1 strain method.

Dislocations are associated with an energy, which is proportional to the square of the length of the Burger's vector. This makes the lowest energy MDs of zinc-blende those with Burger's vectors of type $\frac{a}{2}\langle 110 \rangle$. For a $\langle 100 \rangle$ NW on a (001) substrate, these types of MDs will simultaneously relax strain in two out of the three directions: axial, transverse and out of plane. In the case of a $\langle 110 \rangle$ NW on a (001) substrate, there exist favorable MDs which relax strain in distinctly axial, transverse or out of plane directions as well as MDs which relax all directions simultaneously. This was illustrated in the main text with the model for formation of MDs. The method proposed here is equally well suited for MDs with other directions of Burger's vectors, as the strain associated

with the MD can be defined independently of the MD plane.

V. COMPOSITE PLOTS

Combining the two methods mentioned above (strain +1 and -1) as one composite solution relies on the two solutions producing a consistent solution at the interface. Figure S3 shows resulting strain components at the interface of a simulation of a $\langle 100 \rangle$ type NW on a (001) substrate, where the initial boundary conditions are considered equivalent. The $\langle 110 \rangle$ type NW as well as other strain components were examined as well with similar agreement between methods.

VI. ENERGY RESULTS FOR PLASTIC CONFIGURATIONS

The results of the strain energy integrations for the plastic configurations with the axial MD (MD_{\parallel}) are shown in figure S4. As is evident, the equilibrium configuration at the critical height shows no axial MD (MD_{\parallel}) for the 1% mismatch (a solid line crosses below the unity line first), while for 2%, 3% and 4% the equilibrium configuration at the critical height shows at least one axial MD (a dashed line crosses is the first to cross below the unity line). The results are summarized in the main text.

†: tobias.saerkjaer@nbi.ku.dk, krogstrup@nbi.dk

¹ COMSOL Multiphysics 5.4 Documentation, COMSOL Inc., www.comsol.com/documentation, October 3 2018

² M. E. Levinshtein, S.L. Rumyantsev *Handbook Series on Semiconductor Parameters*, vol.1, M. Levinshtein, S. Rumyantsev and M. Shur, ed., World Scientific, London, 1996, pp. 77-103.

³ M.P. Mikhailova *Handbook Series on Semiconductor Parameters*, vol.1, M. Levinshtein, S. Rumyantsev and M. Shur, ed., World Scientific, London, 1996, pp. 147-168.

⁴ A. K. Head *Edge Dislocations in Inhomogenous Media*, Proc. Phys. Soc. B **66**, 793 (1953)

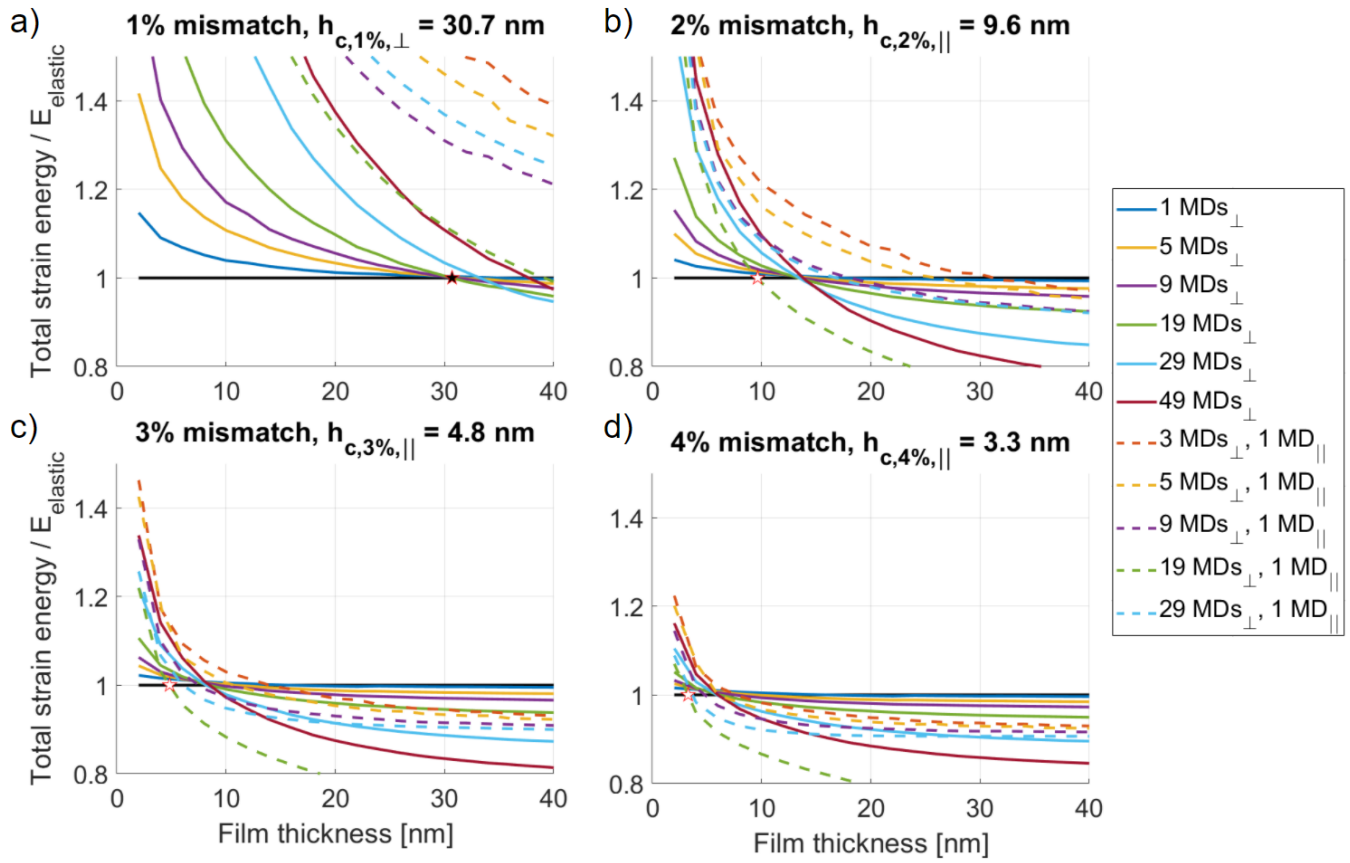


Figure S4: **Strain energy as a function of film thickness.** Each panel shows an examination for a specific mismatch. For each film thickness the favored configuration is the one with the lowest strain energy, and the critical height is found when a plastic configuration crosses below the unity line (first is marked).